Nanoscale Horizons

ROYAL SOCIETY OF CHEMISTRY

COMMUNICATION

View Article Online
View Journal | View Issue

Cite this: *Nanoscale Horiz.*, 2023, 8, 202

Received 16th September 2022,
Accepted 25th November 2022

DOI: 10.1039/d2nh00429a

rsc.li/nanoscale-horizons

Giant thermal switching in ferromagnetic VSe_2 with programmable switching temperature†

Chao Wu,[ab] Yunshan Zhao,[c] Gang Zhang *[d] and Chenhan Liu *[ae]

Active and reversible modulation of thermal conductivity can realize efficient heat energy management in many applications such as thermoelectrics. Using first-principles calculations, this study reports a giant thermal switching ratio of 12, much higher than previously reported values, in monolayer 2H-VSe_2 above room temperature. Detailed analysis indicates that the high thermal switching ratio is dominated by the ferromagnetic ordering induced phonon bandgap, which significantly suppresses the phonon–phonon scattering phase space across the entire vibration spectrum. The thermal switching in bulk 2H-VSe_2 is also investigated and the thermal switching ratio reaches 9.2 at the magnetic transition temperature. Both the phonon–phonon scattering space phase and phonon anharmonicity are responsible for the 9.2-fold thermal switching. This study advances the understanding of heat energy transport in two-dimensional ferromagnets, and also provides new insight into heat energy control and conversion.

New concepts

Ferromagnets are potential candidates for thermal switching since they typically have a high switching ratio of thermal conductivity. However, a high switching ratio is only achieved at low temperature and no switching ratio over 3 has been reported around room temperature. Herein, we report a giant switching ratio of 12 at a magnetic transition temperature of 430 K from the ferromagnetic to paramagnetic phase in monolayer 2H-VSe_2. We also find that the switching ratio in 2H-VSe_2 has a weak dependence on thickness. Combining the fact that the magnetic transition temperature of few-layer 2H-VSe_2 decreases monotonously with increasing thickness, a highly efficient thermal switch with programmable switching temperature can be realized based on few-layer 2H-VSe_2 by simply using an appropriate thickness. These findings advance the understanding of thermal control in ferromagnets and provide a practical way to design thermal switching with a desired working temperature.

Introduction

Thermoelectric materials can convert waste heat into electricity, making them attractive in the field of heat energy harvesting. In order to achieve a high conversion efficiency, a low thermal conductivity is highly desired.[1–5] For example, doping, as an efficient method, has been widely employed to achieve a low thermal conductivity and a high thermoelectric power factor coefficient.[6] On the other hand, for hot-spot thermal management in the field of electronic cooling, one should combine active and passive cooling and both a high power factor and a high thermal conductivity are desired.[7,8] Thus, actively and reversibly controlling the thermal conductivity is a new horizon for efficient heat energy management and conversion.

Compared with electrons, phonons (heat energy carriers) have no mass and charge, *i.e.*, there is a lack of direct connections between phonons and the external environment, making their control much more difficult. Nevertheless, many methods, including structural phase transitions by external stimuli,[9–12] electrochemical ion insertion and removal,[13–15] mechanical stress,[16,17] and charge density redistribution,[18] have been proposed to actively and reversibly control phonon transport or thermal conductivity. For example, in ferroelectric perovskites, structural phase transition or domain wall density change triggered by an electric field,[12,19–21] temperature,[12,22] and substrate strain[23,24] has been employed to explore the reversible

[a] *Micro- and Nano-scale Thermal Measurement and Thermal Management Laboratory, School of Energy and Mechanical Engineering, Nanjing Normal University, Nanjing, 210023, P. R. China. E-mail: chenhanliu@njnu.edu.cn*
[b] *Jiangsu Key Laboratory for Design and Manufacture of Micro-Nano Biomedical Instruments, School of Mechanical Engineering, Southeast University, Nanjing, 211100, P. R. China*
[c] *NNU-SULI Thermal Energy Research Center (NSTER) & Center for Quantum Transport and Thermal Energy Science (CQTES), School of Physics and Technology, Nanjing Normal University, Nanjing 210023, P. R. China*
[d] *Institute of High Performance Computing, Agency for Science, Technology and Research, 138632, Singapore. E-mail: zhangg@ihpc.a-star.edu.sg*
[e] *Jiangsu Key Laboratory for Numerical Simulation of Large-Scale Complex Systems, Nanjing Normal University, Nanjing, 210023, P. R. China*

† Electronic supplementary information (ESI) available. See DOI: https://doi.org/10.1039/d2nh00429a

control of thermal conductivity. Considering the possible technological applications of thermal control, we propose the following two general conditions: (i) the switching ratio should be up to 10; and (ii) the switching temperature or working temperature should be around room temperature. Accordingly, ferromagnets are the most potential material systems for thermal control since they have the highest switching ratio based on published studies.[25–27] However, high thermal switching in ferromagnets typically occurs around the magnetic transition temperature, which is much lower than that occurring at room temperature, making condition (ii) not satisfied. Thus, at present, finding a ferromagnet with a high magnetic transition temperature or increasing the magnetic transition temperature by external stimuli is necessary to realize controllable thermal transport for practical applications.

Compared with bulk ferromagnets, it has been demonstrated that an electric field,[28–30] magnetic field,[31,32] electrostatic doping,[33] and strain[34,35] can significantly modulate the magnetic transition temperature in two-dimensional (2D) ferromagnets. Thus, 2D ferromagnets have a high possibility to realize a high switching ratio around room temperature. Recently, the discovery of various 2D ferromagnets,[36–40] such as CrI_3,[41] and $Cr_2Ge_2Te_6$,[28] has provided the possibility of realizing novel devices with broad applications from sensing to van der Waals spintronics. The thermal switching properties in several 2D ferromagnets were also investigated by first-principles calculations.[42,43] Although these first-principles calculations observed high thermal switching ratios at low temperature, there is no report on thermal switching in 2D ferromagnets around room temperature. Fortunately, a recent experiment reported that ferromagnetic (FM) ordering in monolayer 1T-VSe_2 can persist well above room temperature.[44] A more recent experiment reported that for an 8 nm 2H-VSe_2 thin film, the FM-to-PM (paramagnetic) phase transition temperature can reach $\sim$430 K due to magnetic anisotropy.[45] In addition, with an increase in the thickness, the magnetic transition temperature decreases monotonously from $\sim$430 K to $\sim$300 K at around 50 nm. Therefore, the high magnetic transition temperature from the FM to the PM phase in VSe_2 provides the possibility of realizing a high thermal switching ratio around room temperature.

To address the possibility of thermal switching in VSe_2, in the current study, the switching ratio that originates from the FM–PM phase transition in monolayer and bulk 2H-VSe_2 is investigated using first-principles calculations. The calculation results indicate that at the FM–PM transition temperature of 430 K, the switching ratio in monolayer 2H-VSe_2 reaches up to 12, which is the highest ratio for ferromagnets around and above room temperature. The switching ratio decreases to 9.2 in bulk 2H-VSe_2 along with a decrease of the magnetic transition temperature to 80 K. Our detailed analysis indicates that the high thermal switching ratio is dominated by the large difference in the weighted phonon–phonon scattering phase space (WP3) in monolayer 2H-VSe_2 and both the WP3 and phonon anharmonicity in bulk 2H-VSe_2. This study deepens the understanding of phonon transport in 2D materials and indicates the possibility of 2H-VSe_2 for controllable thermal switching around room temperature.

Results and discussion

The effect of FM ordering on 2H-VSe_2 is firstly reflected in the structural and energy information through relaxing the structures with (FM) and without (PM) spin polarization. The total energy of both monolayer and bulk 2H-VSe_2 (Fig. 1) in the FM phase is lower than that of the corresponding PM phase (Table S1, ESI†), consistent with experimental measurements[45] and previous theoretical calculations.[46,47] The lower energy in the FM phase indicates the preferred stability and FM ordering for 2H-VSe_2. In addition to the difference in energy, FM ordering also alters the lattice constants, bond angles, and atomic positions, as shown in Table S1 (ESI†). For example, the angle $\angle Se_1V_1Se_2$ decreases from 79.816° to 79.682° in monolayer 2H-VSe_2 when FM ordering is included. Thus, for 2H-VSe_2, FM ordering lowers its energy and alters its lattice structure significantly.

Due to the significant change in lattice structure, the effect of FM ordering on 2H-VSe_2 is secondly reflected in the lattice vibration or the phonon dispersion. Since phonon–orbit coupling may be important in quantifying spin–phonon coupling,[48] the phonon dispersion with spin–orbit coupling is also calculated. The calculation results show that spin–orbit coupling has weak effects on the phonon dispersion, especially for the acoustic phonons in 2H-VSe_2 (Fig. S2, ESI†); thus, in the current work, the spin–orbit coupling is ignored. For both monolayer and bulk 2H-VSe_2, FM ordering creates the phonon bandgap due to the upshift of optical phonon modes (Fig. 2), which is also distinctly indicated by the phonon density of states (DOS) and was observed in a previous study.[42] Strain engineering and doping[18,49] are two efficient strategies for modulating the phonon bandgap. Here, we discover that FM ordering is another efficient and non-destructive strategy for modulating the phonon bandgap. As indicated in ref. 50, introducing or enlarging the phonon bandgap can decrease the number of phonon–phonon scattering channels since the conservation of both energy and momentum during the scattering process becomes more difficult to satisfy. Thus, FM ordering may significantly alter the phonon transport properties and thermal conductivity in 2H-VSe_2.

As discussed above, FM ordering has significant effects on the lattice structure and phonon dispersion, both of which are directly related to the phonon thermal conductivity. Thus, based on first-principles calculations using the linearized Boltzmann transport equation, the lattice (phonon) thermal conductivity of FM and PM 2H-VSe_2 was calculated since they are semiconductors and phonons dominate the thermal transport.[45,51] The calculation details are shown in the ESI.† Notably, the ground state of VSe_2 is still under debate. As indicated in ref. 52, estimation of the ground state in VSe_2 is quite tricky and dependent on the functional used as well as the treatment of V d-electrons. The basic reason, we think, is the close energy of the two structures, *i.e.*, 1T-VSe_2 and 2H-Vse_2.

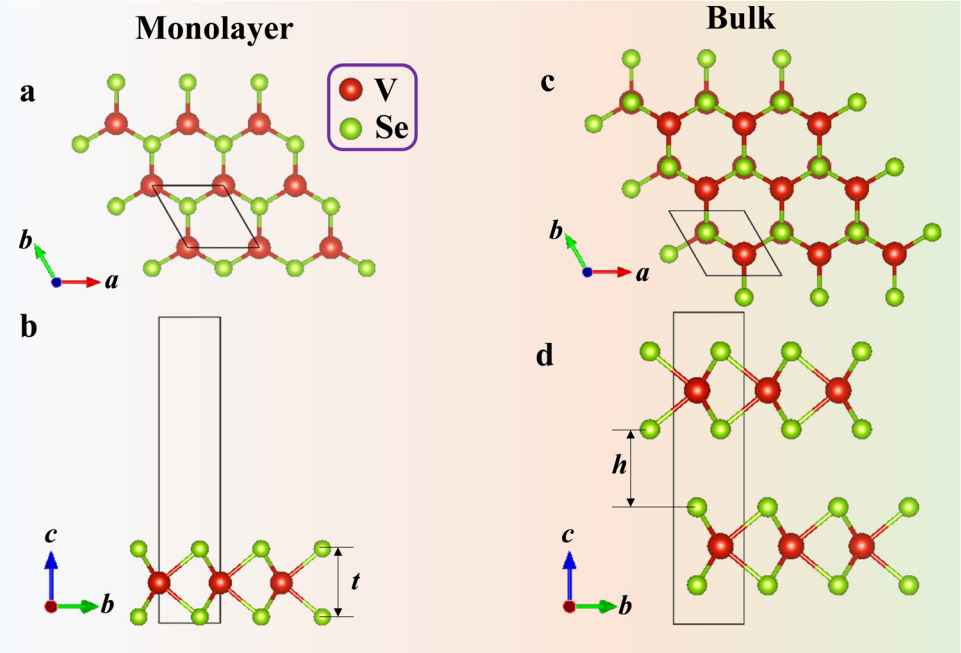

Fig. 1 Atomic structure of monolayer and bulk 2H-VSe_2. The top view (a and c) and side view (b and d) of monolayer and bulk 2H-VSe_2, respectively. The red atoms throughout represent V and the green atoms represent Se. The thickness of monolayer 2H-VSe_2 is defined as the summation of t in (b) and h in (d).

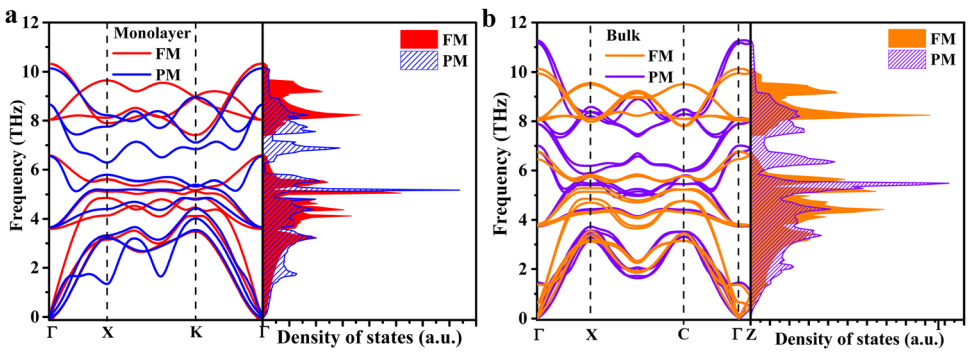

Fig. 2 Phonon dispersion and phonon DOS of 2H-VSe_2. The red and blue lines as well as the orange and purple lines, respectively, represent the FM and PM phases of monolayer (a) and bulk (b) 2H-VSe_2.

In our calculations, the total energy of the 2H structure is just 0.016 eV per unit cell higher than that of the 1T structure. Despite the debate, VSe_2 with the 2H structure has been successfully synthesized[45] and our calculated phonon dispersion of the 2H structure (Fig. 2) has no imaginary frequency, both of which thermodynamically favor the stability of 2H-VSe_2. Thus, the thermal switching in 2H-VSe_2 is considered in the current work. For the magnetic transition temperature T_{FM-PM} from the FM to the PM phase of monolayer 2H-VSe_2, the experimental data of 430 K is directly adopted.[45] Due to the lack of experimental data for bulk 2H-VSe_2, the T_{FM-PM} of 80 K is estimated based on the energy of the spin exchange interaction obtained from the Heisenberg model,[53,54] the details of which are shown in the ESI.† The decrease in the magnetic transition temperature with increasing thickness is consistent with previous experimental measurements.[45] The underlying reason for the decrease indicated by the measurement is the gradual disappearance of magnetic anisotropy with increasing thickness.

From Fig. 3a, the thermal conductivity of both monolayer and bulk 2H-VSe_2 in the PM phase is lower than 5 W m^{-1} K^{-1} around room temperature, indicating the potential for thermoelectric applications.[55,56] As indicated in ref. 57, Se vacancies have important effects on the ferromagnetism in VSe_2. In order to measure the effects of Se vacancies on the ferromagnetism and thermal conductivity in 2H-VSe_2, we perform two comparative calculations. First, we calculate the magnetic moment of the V atom in monolayer 2H-VSe_2, and the calculated results observed were 1.0 μ_B per V atom, which is consistent with previous work.[58] Then, we take two Se atoms away in a $2 \times 2 \times 1$ supercell to mimic the Se vacancies and calculate the magnetic moment of the V atom. Interestingly, the magnetic moment per

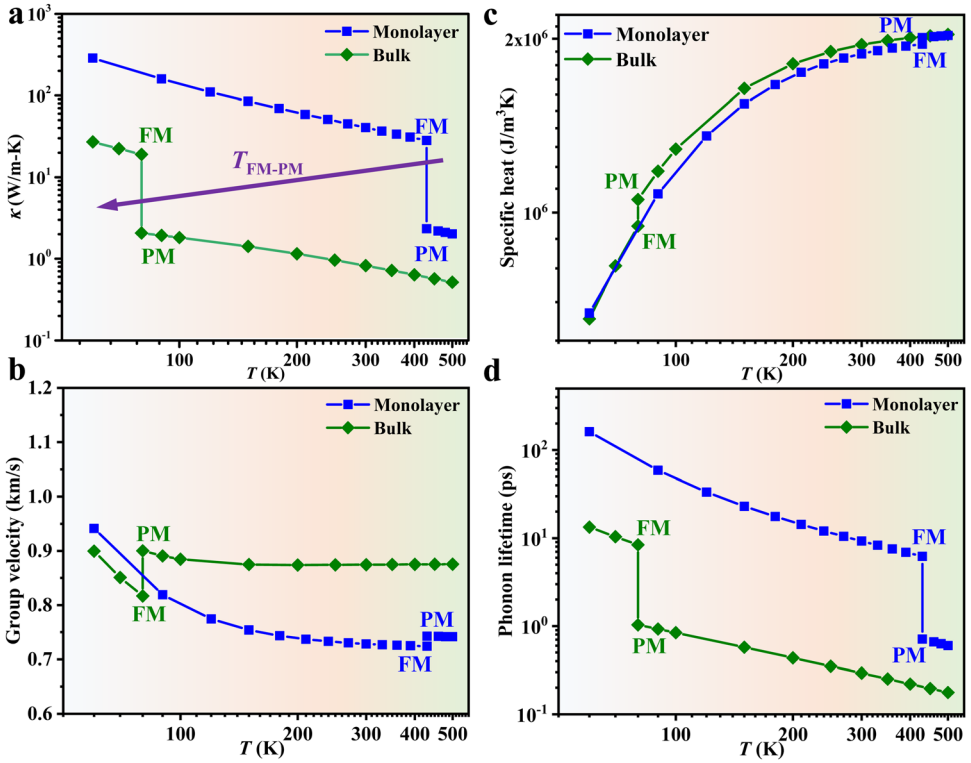

Fig. 3 Phonon transport properties of 2H-VSe_2. The temperature dependent thermal conductivity (a), specific heat averaged group velocity (b), specific heat (c), and specific heat averaged phonon lifetime (d). Throughout, the blue squares represent monolayer 2H-VSe_2 and the olive diamonds represent bulk 2H-VSe_2. The thermal conductivity of both monolayer and bulk 2H-VSe_2 shows a giant change at the magnetic transition temperature. For monolayer 2H-VSe_2, the magnetic transition temperature is 430 K, which decreases to 80 K for bulk 2H-VSe_2.

V atom increases to 1.8 μ_B. Thus, Se vacancies can significantly enhance the ferromagnetism in 2H-VSe_2. For the effects of Se vacancies on the thermal conductivity, vacancies typically decrease the thermal conductivity due to phonon–defect scattering. However, ferromagnetism in 2H-VSe_2 increases the thermal conductivity as shown in Fig. 3a. Thus, there is a competition between Se-vacancy-introduced phonon–defect scattering and enhanced ferromagnetism. The increase or decrease of thermal conductivity in 2H-VSe_2 depends on which one is dominant. This competition is interesting, which deserves further study.

From Fig. 3a, we can also observe that for both monolayer and bulk 2H-VSe_2, the thermal conductivity in the FM phase is much larger than that in the PM phase, *i.e.*, at the T_{FM-PM} of 430 K (80 K) the thermal conductivity of monolayer (bulk) 2H-VSe_2 in the FM phase is about 12 (9.2) times that in the PM phase. Notably, the PM phase in the current study is treated as the non-magnetic (NM) phase. There are two reasons for this treatment: (1) the bulk VSe_2 observed in many experimental studies[59,60] and first-principles calculations predicted the non-magnetic phase in monolayer VSe_2;[61] and (2) if the randomly oriented magnetic moments, namely spin fluctuations, are considered (PM), the thermal conductivity change or the switching ratio at T_{FM-PM} should be even larger since spin fluctuations typically decrease the thermal conductivity.[62] Thus, the large change in thermal conductivity at T_{FM-PM} in the current work represents the lower limit of the switching ratio in 2H-VSe_2. Such a large change in thermal conductivity indicates that FM ordering can significantly improve the phonon transport. A similar phenomenon was also observed in the 2D van der Waals ferromagnets $FeCl_3$, $RuCl_3$, $RuBr_3$, and RuI_3.[43] Interestingly, for 2H-VSe_2, at T_{FM-PM} the high switching ratio of thermal conductivity has a weak dependence on the thickness (Fig. 3a). Combining the fact that the magnetic transition temperature of 2H-VSe_2 decreases monotonously with increasing thickness,[45] a high switching ratio with a programmable switching temperature can be realized by simply employing an appropriate thickness. In order to verify the accuracy of the thermal conductivity and thermal switching ratio, the thermal conductivity of 1T-VSe_2 (Fig. S3, ESI†), the convergence of the number of q points and scalebroad during the solution of the Boltzmann transport equation (Fig. S4, ESI†), and four-phonon effects (Fig. S5, ESI†) are investigated. The details are shown in the ESI.† All these considerations support the findings in the current work. Since the structural parameters of the PM and FM phases are different due to FM ordering, in order to understand the effects of pure structural change and pure magnetic order on the thermal properties, we calculate the phonon dispersion of 2H-VSe_2 using the PM structure with spin polarization. Interestingly, the phonon dispersion of the PM structure with spin polarization is similar to that of the FM structure but is much different from that of

the PM structure without spin polarization (Fig. S6, ESI†), indicating that the giant thermal switching in 2H-VSe_2 is caused mainly by magnetic order while the structural change has weak effects.

Based on kinetic theory, the lattice (phonon) thermal conductivity k is determined by the specific heat C, phonon group velocity v, and phonon lifetime τ, *i.e.*, $k = \Sigma_\lambda C_\lambda v_\lambda^2 \tau_\lambda$, where λ is the phonon mode. Next, we will investigate the effects of these three parameters individually on the thermal conductivity change at T_{FM-PM}. Since v_λ and τ_λ are phonon mode λ dependent parameters, in order to clearly and intuitively show their effects on the thermal conductivity, the specific heat averaged v and τ are calculated as follows:

$$\bar{X} = \frac{\sum_\lambda C_\lambda X_\lambda}{\sum_\lambda C_\lambda} \quad (1)$$

where X denotes v or τ. The specific heat C is calculated by summing C_λ among all the phonon modes, *i.e.*, $C = \sum_\lambda C_\lambda$. Fig. 3b–d, respectively, show the temperature dependent v, C, and τ. Through these three figures, it is obvious that at T_{FM-PM}, both the phonon velocity and specific heat have slight effects on the large change in thermal conductivity for 2H-VSe_2, which instead is dominated by the phonon lifetime. Moreover, these three figures can explain that the slightly lower switching ratio in bulk 2H-VSe_2 is caused by the larger increase in the specific heat (Fig. 3c) and phonon group velocity (Fig. 3b) from the FM to the PM phase, partially eliminating the effects of the phonon lifetime (Fig. 3d). Since the phonon lifetime is dominant and determined by WP3 and phonon anharmonicity, in order to further explore the change in thermal conductivity at T_{FM-PM}, the specific heat averaged WP3 and Grüneisen parameter γ using eqn (1) are then calculated, as shown in Fig. 4. For monolayer 2H-VSe_2, at the T_{FM-PM} of 430 K, the specific heat averaged WP3 in the PM phase is about 9.1 times that in the FM phase (blue square symbols in Fig. 4a). The ratio of the specific heat averaged WP3 between the PM and FM phases is similar to that (8.8) of the specific heat averaged phonon lifetime between the FM and PM phases (Fig. 3d), indicating the dominant role of phonon–phonon scattering phase space on the thermal conductivity change. The much smaller WP3 in the FM phase originates from the FM ordering induced phonon bandgap (blue lines in Fig. 2a), which makes the conservation of both energy and momentum more difficult to satisfy. The much weaker change in specific heat averaged γ at the T_{FM-PM} (blue squares in Fig. 4b) verifies the dominant role of phonon–phonon scattering phase space. For bulk 2H-VSe_2, at the T_{FM-PM} of 80 K, in addition to the phonon–phonon scattering phase space (olive diamond symbols in Fig. 4a), phonon anharmonicity also significantly affects the thermal conductivity change (olive diamonds in Fig. 4b). Quantitatively, the ratio of the specific heat averaged WP3 between the PM and FM phases is 3.1 and the ratio of the specific heat averaged γ between the PM and FM phases is 3.2; thus, the overall ratio combining WP3 and γ between the PM and FM phases is 9.9, which is similar to the ratio of the phonon lifetime (8.2) or thermal conductivity (9.2) between the FM and PM phases for bulk VSe_2.

Although the specific heat averaged τ, WP3, and γ can provide an intuitive explanation for the large change in thermal conductivity at T_{FM-PM}, what is missing is detailed mode dependent information that can provide a deeper understanding about the underlying mechanism of thermal switching. Next, the mode (frequency) dependent τ data are compared at T_{FM-PM} between the FM and PM phases. As shown in Fig. 5, for both monolayer and bulk 2H-VSe_2, at T_{FM-PM} the phonon lifetime in the FM phase is much larger than that in the PM phase over the whole frequency range, indicating that FM ordering can improve phonon transport across the entire vibration spectrum. Such an FM ordering introduced improvement of phonon transport is very different from previous strategies for modulating the thermal conductivity, for which phonons within only a narrow spectrum range can be

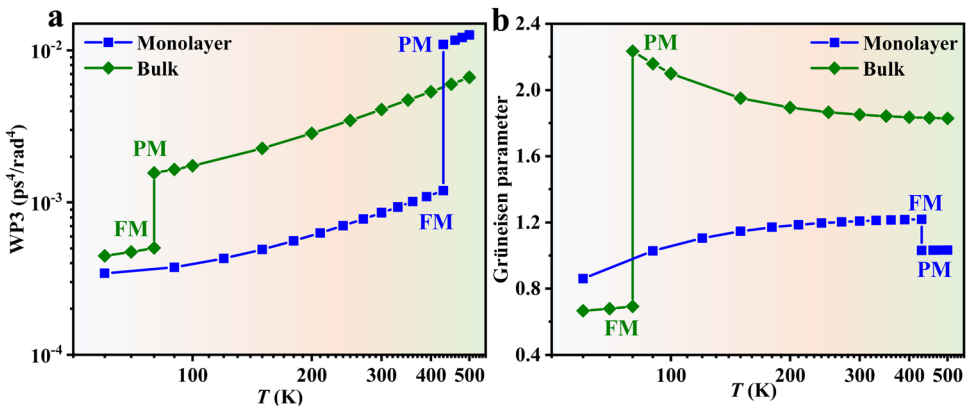

Fig. 4 Specific heat averaged weighted phonon–phonon scattering phase space WP3 (a) and Grüneisen parameter (b) of 2H-VSe_2. Throughout, the blue squares represent monolayer 2H-VSe_2 and the olive diamonds represent bulk 2H-VSe_2. For monolayer 2H-VSe_2, the giant thermal conductivity change at T_{FM-PM} in Fig. 3a is dominated by the giant change in phonon–phonon scattering phase space; by contrast, for bulk 2H-VSe_2, the change in both phonon–phonon scattering phase space and phonon anharmonicity contributes to the change in thermal conductivity at T_{FM-PM}.

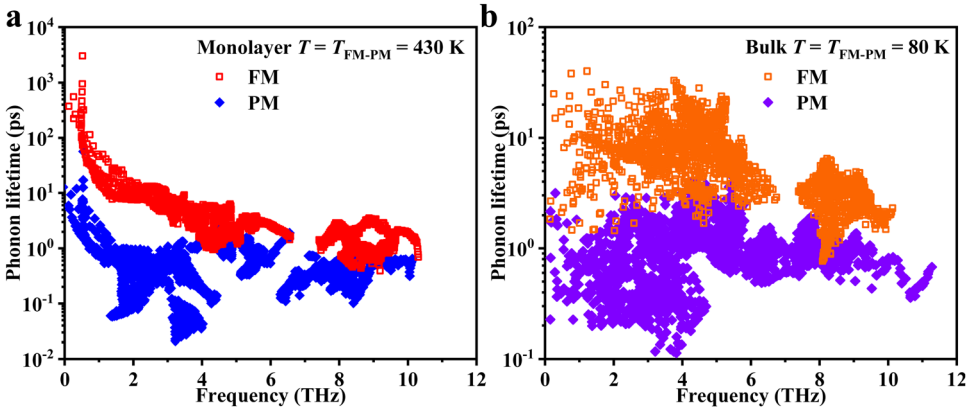

Fig. 5 Phonon lifetime of monolayer (a) and bulk (b) 2H-VSe_2 at the magnetic transition temperature from the FM phase (hollow symbols) to the PM phase (solid symbols).

modulated. The improvement in phonon transport across the entire vibration spectrum is the underlying reason for the giant thermal conductivity change for 2H-VSe_2 at the FM–PM phase transition.

As discussed above, the phonon lifetime is determined by WP3 and phonon anharmonicity. Thus, the mode dependent WP3 and phonon anharmonicity are compared between the FM and PM phases, respectively. For monolayer 2H-VSe_2, the mode dependent WP3 in the PM phase is about 10 times that in the FM phase over the whole frequency range (Fig. 6a), verifying the dominant role of phonon–phonon scattering phase space in the thermal conductivity change indicated in Fig. 4a as well as the significant effects of the enlarged phonon bandgap on thermal switching (Fig. 2a). By contrast, for bulk 2H-VSe_2, the difference in the mode dependent WP3 data between the FM and PM phases is much smaller (Fig. 6b) since the phonon anharmonicity also contributes significantly to the large thermal conductivity change at T_{FM-PM}, which is verified by the mode dependent γ in Fig. 6d. Therefore, for the monolayer 2D ferromagnet 2H-VSe_2, the phonon–phonon scattering phase space dominates the thermal conductivity change at the magnetic transition temperature, whereas for bulk 2H-VSe_2, both

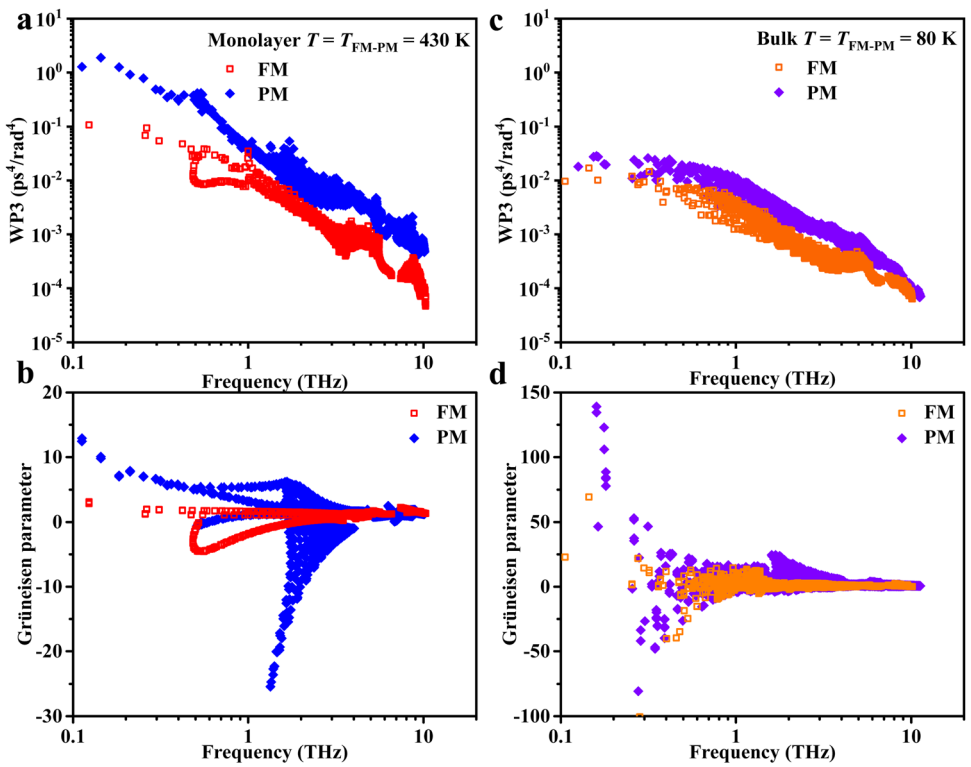

Fig. 6 Phonon frequency dependent WP3 (a and c) and Grüneisen parameter (b and d) for monolayer and bulk 2H-VSe_2 at the magnetic phase transition temperature, respectively. Throughout, the hollow symbols denote the FM phase and the solid symbols denote the PM phase.

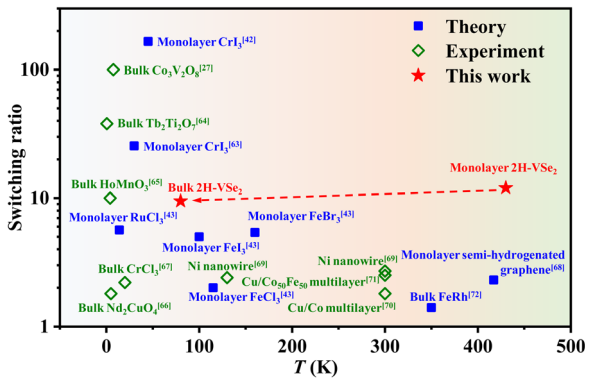

Fig. 7 Temperature dependent switching ratio of thermal conductivity in ferromagnets.[27,42,43,63–72]

the phonon–phonon scattering phase space and phonon anharmonicity control the thermal conductivity change at the magnetic transition temperature.

Based on the above discussion, 2H-VSe_2 has a giant switching ratio of thermal conductivity. Fig. 7 compares the temperature dependent switching ratio values for some ferromagnets. Notably, the solid symbols represent the theoretical data while the hollow symbols represent the experimental data. As shown in this figure, although a high switching ratio can be obtained at low temperature, a switching ratio of over 3 around room temperature has never been reported in previous literature, either theoretically or experimentally. For example, through magnetic field induced magnetization vector alignment from antiparallel to parallel, a switching ratio of only 2.5 was experimentally obtained at 300 K for $Cu/Co_{50}Fe_{50}$ multilayer films,[71] and a small switching ratio of 1.4 was theoretically predicted for bulk FeRh at 340 K.[72] Our work predicts a giant switching ratio of 12 at 430 K and 9.2 at 80 K. Based on the experimental data, the magnetic transition temperature from the FM to the PM phase for few-layer 2H-VSe_2 can be modulated *via* the thickness. Combining the fact that the switching ratio shows only a slight decrease with increasing thickness (the dashed red line in Fig. 7), a giant switching ratio at a desired working temperature can be obtained using an appropriate thickness.

Conclusions

In summary, this study reports giant thermal switching in the 2D ferromagnet 2H-VSe_2 using first-principles calculations with the linearized Boltzmann transport equation. For monolayer 2H-VSe_2, the thermal conductivity at the magnetic transition temperature of 430 K from the PM to the FM phase jumps 12-fold, which originates from the FM ordering induced drop in phonon–phonon scattering phase space. For bulk 2H-VSe_2, the thermal switching ratio is 9.2 at the magnetic transition temperature of 80 K, where both the phonon–phonon scattering phase space and phonon anharmonicity contribute to the thermal conductivity change. Since both monolayer and bulk 2H-VSe_2 has a giant switching ratio and the magnetic transition temperature can be designed by simply changing the thickness, this study discovers a material that can meet two important factors – *i.e.*, a high switching ratio and a switching temperature around room temperature – for thermal switching, which indicates the high possibility of realizing controllable thermal transport.

Data availability statement

The data will be made available from the corresponding author upon reasonable request.

Author contributions

C. Liu initiated the project. C. Wu performed the calculations and C. Liu wrote the manuscript. C. Liu and G. Zhang supervised the project. G. Zhang and Y. Zhao edited the manuscript. All authors discussed the results and commented on the manuscript.

Conflicts of interest

There are no conflicts to declare.

Acknowledgements

This work was supported by the National Natural Science Foundation of China (Grant no. 52206092) and the Natural Science Foundation of Jiangsu Province (Grant no. BK20210565). C. H. Liu was funded by the Department of Science and Technology of Jiangsu Province (BK20220032), the Basic Science (Natural Science) Research Project of Higher Education Institutions of Jiangsu Province (21KJB470009) and the "Shuangchuang" Doctor program of Jiangsu Province (JSSCBS20210315). C. H. Liu was also funded by the Nanjing Science and Technology Innovation Project for Overseas Students and open research fund of Jiangsu Key Laboratory for Design and Manufacture of Micro-Nano Biomedical Instruments, Southeast University (No. KF202010). Y. Zhao is supported by the Natural Science Foundation of Jiangsu Province (Grant no. BK20210556) and the Jiangsu Specially-Appointed Professor Program. The authors thank the Scientific Computing Center of Nanjing Normal University and the Big Data Center of Southeast University for performing the numerical calculations presented in this paper.

References

1 W. K. He, D. Y. Wang, H. J. Wu, Y. Xiao, Y. Zhang, D. S. He, Y. Feng, Y. J. Hao, J. F. Dong, R. Chetty, L. J. Hao, D. F. Chen, J. F. Qin, Q. Yang, X. Li, J. M. Song, Y. C. Zhu, W. Xu, C. L. Niu, X. Li, G. T. Wang, C. Liu, M. Ohta, S. J. Pennycook, J. Q. He, J. F. Li and L. D. Zhao, *Science*, 2019, **365**, 1418–1424.

2 J. Mao, H. T. Zhu, Z. W. Ding, Z. H. Liu, G. A. Gamage, G. Chen and Z. F. Ren, *Science*, 2019, **365**, 495–498.

3 S. Roychowdhury, T. Ghosh, R. Arora, M. Samanta, L. Xie, N. K. Singh, A. Soni, J. Q. He, U. V. Waghmare and K. Biswas, *Science*, 2021, **371**, 722–727.
4 X. W. Zhang, Y. Guo, Z. B. Zhou, Y. H. Li, Y. F. Chen and J. L. Wang, *Energy Environ. Sci.*, 2021, **14**, 4059–4066.
5 X. W. Zhang, C. H. Liu, Y. Tao, Y. H. Li, Y. L. Guo, Y. F. Chen, X. C. Zeng and J. L. Wang, *Adv. Funct. Mater.*, 2020, **30**, 2001200.
6 G. Zhang and B. W. Li, *Nanoscale*, 2010, **2**, 1058–1068.
7 J. Mao, G. Chen and Z. Ren, *Nat. Mater.*, 2021, **20**, 454–461.
8 M. Zebarjadi, *Appl. Phys. Lett.*, 2015, **106**, 203506.
9 Q. Y. Lu, S. Huberman, H. T. Zhang, Q. C. Song, J. Y. Wang, G. Vardar, A. Hunt, I. Waluyo, G. Chen and B. Yildiz, *Nat. Mater.*, 2020, **19**, 655–662.
10 R. Shrestha, Y. X. Luan, S. Shin, T. Zhang, X. Luo, J. S. Lundh, W. Gong, M. R. Bockstaller, S. Choi, T. F. Luo, R. K. Chen, K. Hippalgaonkar and S. Shen, *Sci. Adv.*, 2019, **5**, eaax3777.
11 J. Shin, J. Sung, M. Kang, X. Xie, B. Lee, K. M. Lee, T. J. White, C. Leal, N. R. Sottos, P. V. Braun and D. G. Cahill, *Proc. Natl. Acad. Sci. U. S. A.*, 2019, **116**, 5973–5978.
12 K. Aryana, J. A. Tomko, R. Gao, E. R. Hoglund, T. Mimura, S. Makarem, A. Salanova, M. S. Bin Hoque, T. W. Pfeifer, D. H. Olson, J. L. Braun, J. Nag, J. C. Read, J. M. Howe, E. J. Opila, L. W. Martin, J. F. Ihlefeld and P. E. Hopkins, *Nat. Commun.*, 2022, **13**, 1–9.
13 J. Cho, M. D. Losego, H. G. Zhang, H. Kim, J. M. Zuo, I. Petrov, D. G. Cahill and P. V. Braun, *Nat. Commun.*, 2014, **5**, 1–6.
14 G. H. Zhu, J. Liu, Q. Y. Zheng, R. G. Zhang, D. Y. Li, D. Banerjee and D. G. Cahill, *Nat. Commun.*, 2016, **7**, 1–9.
15 A. Sood, F. Xiong, S. D. Chen, H. T. Wang, D. Selli, J. S. Zhang, C. J. McClellan, J. Sun, D. Donadio, Y. Cui, E. Pop and K. E. Goodson, *Nat. Commun.*, 2018, **9**, 1–9.
16 X. H. Meng, T. Pandey, J. Jeong, S. Y. Fu, J. Yang, K. Chen, A. Singh, F. He, X. C. Xu, J. S. Zhou, W. P. Hsieh, A. K. Singh, J. F. Lin and Y. G. Wang, *Phys. Rev. Lett.*, 2019, **122**, 155901.
17 C. H. Liu, Z. Y. Wei, W. Y. Chen, K. D. Bi, J. K. Yang and Y. F. Chen, *Phys. Lett. A*, 2016, **380**, 248–254.
18 G. Z. Qin, Z. Z. Qin, S. Y. Yue, Q. B. Yan and M. Hu, *Nanoscale*, 2017, **9**, 7227–7234.
19 C. H. Liu, Y. F. Chen and C. Dames, *Phys. Rev. Appl.*, 2019, **11**, 044002.
20 C. H. Liu, V. Mishra, Y. F. Chen and C. Dames, *Adv. Theory Simul.*, 2018, **1**, 1800098.
21 C. H. Liu, P. Lu, Z. Z. Gu, J. K. Yang and Y. F. Chen, *J. Phys. Chem. C*, 2020, **124**, 26144–26152.
22 M. Tachibana, T. Kolodiazhnyi and E. Takayama-Muromachi, *Appl. Phys. Lett.*, 2008, **93**, 092902.
23 E. Langenberg, D. Saha, M. E. Holtz, J.-J. Wang, D. Bugallo, E. Ferreiro-Vila, H. Paik, I. Hanke, S. Ganschow, D. A. Muller, L.-Q. Chen, G. Catalan, N. Domingo, J. Malen, D. G. Schlom and F. Rivadulla, *Nano Lett.*, 2019, **19**, 7901–7907.
24 S. Ning, S. C. Huberman, C. Zhang, Z. Zhang, G. Chen and C. A. Ross, *Phys. Rev. Appl.*, 2017, **8**, 054049.
25 L. Chenhan and C. Yunfei, *Sci. China: Phys., Mech. Astron.*, 2022, **65**, 117009.
26 C. H. Liu, Q. Fu, Z. Z. Gu and P. Lu, *Phys. Chem. Chem. Phys.*, 2020, **22**, 22016–22022.
27 X. Zhao, J. C. Wu, Z. Y. Zhao, Z. Z. He, J. D. Song, J. Y. Zhao, X. G. Liu, X. F. Sun and X. G. Li, *Appl. Phys. Lett.*, 2016, **108**, 242405.
28 I. A. Verzhbitskiy, H. Kurebayashi, H. Cheng, J. Zhou, S. Khan, Y. P. Feng and G. Eda, *Nat. Electron.*, 2020, **3**, 460–465.
29 B. Huang, G. Clark, D. R. Klein, D. MacNeill, E. Navarro-Moratalla, K. L. Seyler, N. Wilson, M. A. McGuire, D. H. Cobden, D. Xiao, W. Yao, P. Jarillo-Herrero and X. D. Xu, *Nat. Nanotechnol.*, 2018, **13**, 544–548.
30 R. Z. Xu and X. L. Zou, *J. Phys. Chem. Lett.*, 2020, **11**, 3152–3158.
31 A. McCreary, T. T. Mai, F. G. Utermohlen, J. R. Simpson, K. F. Garrity, X. Z. Feng, D. Shcherbakov, Y. L. Zhu, J. Hu, D. Weber, K. Watanabe, T. Taniguchi, J. E. Goldberger, Z. Q. Mao, C. N. Lau, Y. M. Lu, N. Trivedi, R. V. Aguilar and A. R. H. Walker, *Nat. Commun.*, 2020, **11**, 1–8.
32 Z. Wang, I. Gutierrez-Lezama, N. Ubrig, M. Kroner, M. Gibertini, T. Taniguchi, K. Watanabe, A. Imamoglu, E. Giannini and A. F. Morpurgo, *Nat. Commun.*, 2018, **9**, 1–8.
33 S. W. Jiang, L. Z. Li, Z. F. Wang, K. F. Mak and J. Shan, *Nat. Nanotechnol.*, 2018, **13**, 549–553.
34 X. H. Hu, Y. H. Zhao, X. D. Shen, A. V. Krasheninnikov, Z. F. Chen and L. T. Sun, *ACS Appl. Mater. Interfaces*, 2020, **12**, 26367–26373.
35 A. M. Leon, J. W. Gonzalez, J. Mejia-Lopez, F. C. de Lima and E. S. Morell, *2D Mater.*, 2020, **7**, 035008.
36 C. Gong, L. Li, Z. L. Li, H. W. Ji, A. Stern, Y. Xia, T. Cao, W. Bao, C. Z. Wang, Y. A. Wang, Z. Q. Qiu, R. J. Cava, S. G. Louie, J. Xia and X. Zhang, *Nature*, 2017, **546**, 265–269.
37 Z. Y. Fei, B. Huang, P. Malinowski, W. B. Wang, T. C. Song, J. Sanchez, W. Yao, D. Xiao, X. Y. Zhu, A. F. May, W. D. Wu, D. H. Cobden, J. H. Chu and X. D. Xu, *Nat. Mater.*, 2018, **17**, 778–782.
38 A. M. Tokmachev, D. V. Averyanov, O. E. Parfenov, A. N. Taldenkov, I. A. Karateev, I. S. Sokolov, O. A. Kondratev and V. G. Storchak, *Nat. Commun.*, 2018, **9**, 1–9.
39 H. Kumar, N. C. Frey, L. Dong, B. Anasori, Y. Gogotsi and V. B. Shenoy, *ACS Nano*, 2017, **11**, 7648–7655.
40 C. Long, T. Wang, H. Jin, H. Wang and Y. Dai, *J. Phys. Chem. Lett.*, 2020, **11**, 2158–2164.
41 B. Huang, G. Clark, E. Navarro-Moratalla, D. R. Klein, R. Cheng, K. L. Seyler, D. Zhong, E. Schmidgall, M. A. McGuire, D. H. Cobden, W. Yao, D. Xiao, P. Jarillo-Herrero and X. D. Xu, *Nature*, 2017, **546**, 270–273.
42 G. Z. Qin, H. M. Wang, L. C. Zhang, Z. Z. Qin and M. Hu, *J. Mater. Chem. C*, 2020, **8**, 3520–3526.
43 Y. Q. Liu, Q. X. Liu, Y. Liu, X. Jiang, X. L. Zhang and J. J. Zhao, *Nanoscale*, 2021, **13**, 7714–7722.
44 M. Bonilla, S. Kolekar, Y. J. Ma, H. C. Diaz, V. Kalappattil, R. Das, T. Eggers, H. R. Gutierrez, M. H. Phan and M. Batzill, *Nat. Nanotechnol.*, 2018, **13**, 289–293.
45 X. Wang, D. A. Li, Z. J. Li, C. Z. Wu, C. M. Che, G. Chen and X. D. Cui, *ACS Nano*, 2021, **15**, 16236–16241.

46 A. H. M. A. Wasey, S. Chakrabarty and G. P. Das, *J. Appl. Phys.*, 2015, **117**, 064313.
47 H. R. Fuh, B. H. Yan, S. C. Wu, C. Felser and C. R. Chang, *New J. Phys.*, 2016, **18**, 113038.
48 D. Staros, G. Hu, J. Tiihonen, R. Nanguneri, J. Krogel, M. C. Bennett, O. Heinonen, P. Ganesh and B. Rubenstein, *J. Chem. Phys.*, 2022, **156**, 014707.
49 J. W. Jiang, *Nanoscale*, 2014, **6**, 8326–8333.
50 L. Lindsay, D. A. Broido and T. L. Reinecke, *Phys. Rev. Lett.*, 2013, **111**, 025901.
51 T. G. Park, B. K. Choi, J. Park, J. Kim, Y. J. Chang and F. Rotermund, *ACS Nano*, 2021, **15**, 7756–7764.
52 Z. Popov, N. Mikhaleva, M. Visotin, A. Kuzubov, S. Entani, H. Naramoto, S. Sakai, P. Sorokin and P. Avramov, *Phys. Chem. Chem. Phys.*, 2016, **18**, 33047–33052.
53 H.-R. Fuh, C.-R. Chang, Y.-K. Wang, R. F. L. Evans, R. W. Chantrell and H.-T. Jeng, *Sci. Rep.*, 2016, **6**, 32625.
54 W. Nolting and A. Ramakanth, *Quantum theory of magnetism*, Springer Science & Business Media, 2009.
55 J. Li, X. Y. Zhang, Z. W. Chen, S. Q. Lin, W. Li, J. H. Shen, I. T. Witting, A. Faghaninia, Y. Chen, A. Jain, L. D. Chen, G. J. Snyder and Y. Z. Pei, *Joule*, 2018, **2**, 976–987.
56 T. Wang, C. Zhang, H. Snoussi and G. Zhang, *Adv. Funct. Mater.*, 2020, **30**, 1906041.
57 W. Yu, J. Li, T. S. Herng, Z. Wang, X. Zhao, X. Chi, W. Fu, I. Abdelwahab, J. Zhou and J. Dan, *Adv. Mater.*, 2019, **31**, 1903779.
58 G. V. Pushkarev, V. G. Mazurenko, V. V. Mazurenko and D. W. Boukhvalov, *Phys. Chem. Chem. Phys.*, 2019, **21**, 22647–22653.
59 P. M. Coelho, K. Nguyen Cong, M. Bonilla, S. Kolekar, M.-H. Phan, J. Avila, M. C. Asensio, I. I. Oleynik and M. Batzill, *J. Phys. Chem. C*, 2019, **123**, 14089–14096.
60 A. O. Fumega, M. Gobbi, P. Dreher, W. Wan, C. González-Orellana, M. Peña-Díaz, C. Rogero, J. Herrero-Martín, P. Gargiani and M. Ilyn, *J. Phys. Chem. C*, 2019, **123**, 27802–27810.
61 L. Yin, T. Berlijn, R. Juneja, L. Lindsay and D. S. Parker, *Phys. Rev. B*, 2022, **106**, 085117.
62 X. Zhao, J. Wu, Z. Zhao, Z. He, J. Song, J. Zhao, X. Liu, X. Sun and X. Li, *Appl. Phys. Lett.*, 2016, **108**, 242405.
63 K. Wang, W. X. Zhou, Y. A. Cheng, M. Zhang, H. Wang and G. Zhang, *Nanoscale*, 2021, **13**, 10882–10890.
64 Q. J. Li, Z. Y. Zhao, C. Fan, F. B. Zhang, H. D. Zhou, X. Zhao and X. F. Sun, *Phys. Rev. B: Condens. Matter Mater. Phys.*, 2013, **87**, 214408.
65 X. M. Wang, C. Fan, Z. Y. Zhao, W. Tao, X. G. Liu, W. P. Ke, X. Zhao and X. F. Sun, *Phys. Rev. B: Condens. Matter Mater. Phys.*, 2010, **82**, 094405.
66 R. Jin, Y. Onose, Y. Tokura, D. Mandrus, P. Dai and B. C. Sales, *Phys. Rev. Lett.*, 2003, **91**, 146601.
67 C. A. Pocs, I. A. Leahy, H. Zheng, G. Cao, E.-S. Choi, S. H. Do, K.-Y. Choi, B. Normand and M. Lee, *Phys. Rev. Res.*, 2020, **2**, 013059.
68 H. Q. Li, P. Zhang, T. Ouyang, H. M. Wang, J. Li, C. Y. He, C. X. Zhang and C. Tang, *Appl. Phys. Lett.*, 2022, **120**, 092403.
69 H. T. Huang, M. F. Lai, Y. F. Hou and Z. H. Wei, *Nano Lett.*, 2015, **15**, 2773–2779.
70 J. Kimling, R. B. Wilson, K. Rott, J. Kimling, G. Reiss and D. G. Cahill, *Phys. Rev. B: Condens. Matter Mater. Phys.*, 2015, **91**, 144405.
71 H. Nakayama, B. Xu, S. Iwamoto, K. Yamamoto, R. Iguchi, A. Miura, T. Hirai, Y. Miura, Y. Sakuraba, J. Shiomi and K. Uchida, *Appl. Phys. Lett.*, 2021, **118**, 042409.
72 C. Cazorla and R. Rurali, *Phys. Rev. B*, 2022, **105**, 104401.

